



UPSTREAM TURBULENCE EFFECTS IN THE SPATIO-TEMPORAL CHARACTERISTICS OF A MODEL A-PILLAR VORTEX

Faisal Affejee

Institut Pprime, UPR CNRS 3346, ENSMA, Université de Poitiers,
BP 40109, 86961 Futuroscope Chasseneuil Cedex, France
faisal.affejee@univ-poitiers.fr

Christophe Sicot

Institut Pprime, UPR CNRS 3346, ENSMA, Université de Poitiers,
christophe.sicot@ensma.fr

Rodolphe Perrin

Institut Pprime, UPR CNRS 3346, ENSMA, Université de Poitiers,
rodolphe.perrin@univ-poitiers.fr

Jacques Borée

Institut Pprime, UPR CNRS 3346, ENSMA, Université de Poitiers,
jacques.boree@ensma.fr

ABSTRACT

Conical vortices generated over surfaces having a swept angle with the incidence wind are found in a large class of practical applications. The study presented in this paper is related to the aerodynamic and aero-acoustic of passenger vehicles. More particularly, we focus on the A-pillar vortex, arising on the corner edge, between the windshield and the front side window. The incoming flow fields encountered by passenger cars is highly turbulent due to the natural wind or other road traffic. The goal of the paper is then twofold: (i) educe the spatial and temporal characteristics of the A-pillar conical vortex, (ii) investigate the influence of a turbulent stream on these characteristics. For that purpose, a database of simultaneous stereoscopic HS-PIV and fluctuating wall pressure measurements was compiled. A spectral analysis of the fluctuating pressure under the vortex is used to analyze the link between the unsteady aerodynamics and the wall pressure field. It has been observed a significant amplification of the meandering of the structure highlighting the high receptivity of this structure to perturbations generated by external turbulence.

Introduction

Conical vortices generated over surfaces having a swept angle with the incidence wind are found in a particularly large class of practical applications as aerodynamics (delta-wings), civil engineering and transport engineering. The study presented in this paper has a strong link with the aerodynamic and aero-acoustic of passenger vehicles. More particularly, we focus on the A-pillar vortex, arising on the corner edge, between the windshield and the

front side window. Previous studies (Alam et al., 2003) have shown that the fluctuating pressures in the A-pillar region of a passenger car are the primary source of "in cabin" aerodynamic noise. Indeed, the wall stresses induced by the A-pillar vortex are sufficient to make the front side window vibrate and generate noise disturbances inside the car (Levy and al., 2013). The particularity of these A-pillar structures is their strong interaction with the lateral wall of the car. This differs, for example, from delta-wings leading edge vortices at high angle of attack. A mirror image can be used to qualitatively understand the mean downstream evolution of these structures of concentrated vorticity that shift to the roof when traveling toward the back of the car (Hucho 1998). Most of the work related to these typical structures has been experimental and led in wind tunnel in flows with low levels of free stream turbulence (FST). However, incoming flow fields encountered by passenger car are highly turbulent due to the natural wind or other road traffic. This study is then more focused on the effects of free-stream turbulence on this conical vortex structure. Effects of FST on bluff body aerodynamic have been studied for a long time. Bearman and Morel (1983) described three basic mechanisms by which FST and the mean flow over bluff bodies interact: accelerated transition to turbulence in shear layers, enhanced mixing and entrainment and distortion of FST itself by the mean flow. In this way, this work is a continuation of the work already carried out in the laboratory by Hoarau et al. (2008) which led experiments coupling wall pressure measurements with Doppler Laser Anemometry in a uniform and laminar stream. The analysis of fluctuating pressure spectra have shown two principal contributions which may correspond to a global meander-

ing of the structure and to large scale perturbations generated during the rolling-up of the unsteady vortex sheet. In this paper, we present and discuss results of a similar experiment conducted in a uniform stream and in a turbulent free stream. Bearman and Morel (1983) showed that if the integral length scale of the FST is very large with respect to the body dimension, FST will appear to the local flow as a correlated unsteady mean flow varying magnitude and direction. In this case, the two turbulent fields (free stream and local) will not interact and the effect of FST can be estimated using a quasi-steady assumption. In order to avoid this situation and to focus our study on the interaction between the FST and the A-pillar vortex, two grid generated turbulence were used. The grid generated turbulence intensity of 4% (resp. 2%) at the nose of the body with an integral scale of order of the roll-up width (resp. half of the roll-up width) at the end of the A-pillar. The first section presents the experimental set-up. Following sections deal with the analysis of the effects of external turbulence on the global flow topology of A-pillar vortex with the spatio-temporal properties of the flow.

Experimental Setup

The experiments were performed in a closed loop wind tunnel with octagonal test section ($1m^2$). A dihedron (800mm long, 220mm high) has been chosen as an adequate configuration to reproduce the generic feature of the A-pillar vortex flow (Hoarau, 2008). The two lateral sides are inclined at 10° while the angle of the forward facing ramp is 30° (Fig.1). A rough strip, having 20mm width, (using carborundum of $400\mu m$ height) was positioned across the width of the front side, 5mm from the nozzle to trigger a turbulent boundary layer. The free stream velocity is fixed and equal to $30 m.s^{-1}$. The Reynolds number, based on the square root of the cross section is $4.1e5$. As our motivation was here to minimize interactions with the ground, the body is placed at the center of the test section in order to place it outside the boundary layer. Without any added setup, the free stream turbulence level in the test section is less than 0.2 % at the body location. Higher turbulence levels have been classically generated in the test section using square mesh biplanar grids mounted at the entrance of the test section (Comte-Bellot & Corrsin (1966)). Cross-wire measurements showed that at the body's location (without the body) the longitudinal turbulence intensity (Tu) is equal to 4 % and 2%. Longitudinal velocity autocorrelation measurements led, via Taylor's hypothesis, to an integral scale of the order of magnitude of the conical vortex width at the top of the ramp ($0.14H$, H being the height of the model) for $Tu=4\%$ and about 2 times less for $Tu=2\%$.

The measurement of the surface fluctuating pressure are obtained with off-set sensors because the distance between pressure holes can be much smaller than the one achieved with flush mounted sensors. Those sensors are differential with a bandwidth of [0Hz-1.8kHz] and a pressure range of 250Pa and 1250Pa. The signal recorder is able to simultaneously acquire 30 pressure probe signals with an effective sampling frequency of 6.25 kHz and a cut-off frequency of the anti-aliasing filters set at 2 kHz. Figure 1 presents the pressure taps located in vertical line L_2 (located at a distance from the nozzle of the model equal to $x/H = 1.13$). On this line, the position of pressure taps is indicated depending on $\frac{\epsilon}{\epsilon_0}$ where ϵ is the distance between the pressure taps and the sharp "A-pillar" and ϵ_0 represents

the mean reattachment distance. The location of this mean reattachment was estimated from oil flow visualization, not presented here.

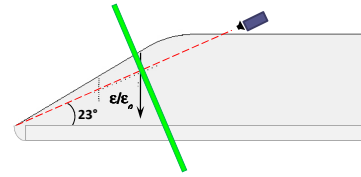


Figure 1. Schematic view of the model. The green sheet corresponds to the 2D-3C PIV measurement plane

HS-PIV systems have been used to record images of particles having a mean diameter of $1 \mu m$. Illumination is provided by a New Wave PEGASUS Laser emitting two pulses of 10mJ (laser sheet thickness $\leq 1mm$). About 24 000 velocity fields were acquired with a PHOTRON ABX-RS camera in a plane normal to the vortex axis (figure 1). A multipass algorithm with a final interrogation window size of 16×16 pixels² and 50% overlapping is applied. Spurious velocities are identified and replaced using both peak ratio and median filters.

Global flow topology

In a previous study Gouveia et al. (2009), using oil and smoke flow visualizations and wall pressure signature, have shown that the A-pillar vortex flow, without FST, consists of a primary and a secondary vortex (figure 2). This secondary vortex, located inside a recirculation zone, is generated by the adverse pressure gradient at the wall due to the interaction between the primary vortex and the wall (Levy et al.(2013)).

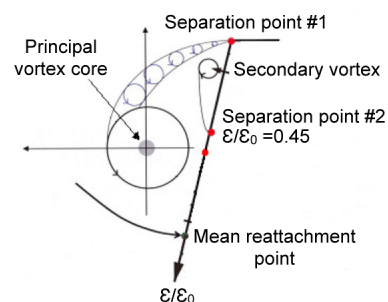


Figure 2. Scheme of the A-pillar vortex and pressure tap positions. ϵ_0 represents the mean reattachment distance.

The addition of a FST has a great impact on the global flow topology. We consider first, its influence on fluctuating wall pressure signal. Figure 3 presents the evolution of the fluctuating pressure coefficient, C_p' , along the $\frac{\epsilon}{\epsilon_0}$ axis, located in the same plane as the Stereo-PIV (figure 1). The data of figure 3 show a very profound influence of FST. The global level is largely higher than in the absence of FST.

In the uniform free-stream case, one maxima is observed located at $\frac{\epsilon}{\epsilon_0} = 0.44$. This point, corresponding to the maximum adverse pressure gradient, is located at the detachment point where the primary vortex creates the secondary vortex by extracting vorticity from the wall. With Levy et al. (2013), one may conclude that this high level of fluctuations is created by the fluctuations of the second separation point. In the presence of FST, we observe that a second local maximum, located near the point where the primary vortex impinges the wall ($\frac{\epsilon}{\epsilon_0} = 0.79$), is arising. One may suppose that these maxima are due to the spatial fluctuation of the primary vortex enhanced by the presence of FST. This hypothesis will be confirmed by the study of the spatial motion of the structure presented later. Moreover, the global increase of C'_p in the case of FST, even for pressure sensors located near the edge of the body ($\frac{\epsilon}{\epsilon_0} < 0.2$ in figure 3), indicates that instantaneous fluctuations of the vorticity sheet separating over the A-pillar induce strong fluctuations of the pressure field, enhanced in the presence of FST. The main factors influencing the fluctuating pressure profile are namely the 3D flapping of the separating vorticity sheet and the primary (impingement) or secondary (separation) interaction of the vorticity sheet with the side wall. These factors are of course globally coupled over the full length of the conical structure. Indeed, the structure has been observed to behave as a wave guide for given ranges of frequencies (see Hoarau et al 2008). Figure 4 presents the mean vorticity fields obtained with and without FST. One may observe that they are very similar. In particular, the mean position of the vortex seems to be unchanged by the presence of FST. One may notice a decrease of the vorticity level and an important increase of the turbulent kinetic energy at the center of the structure. Table 1 shows that both Reynolds stresses react in a very different way to the increase of external turbulence. Particularly at the vortex center where the u^2 and w^2 contributions are quite unchanged while v^2 contribution, quasi parallel to the wall, is greatly enhanced. An examination of instantaneous velocity fields in the presence of FST shows in fact that such an increase of v^2 and of the anisotropy is due to a flapping of very large amplitude of the separating shear layer

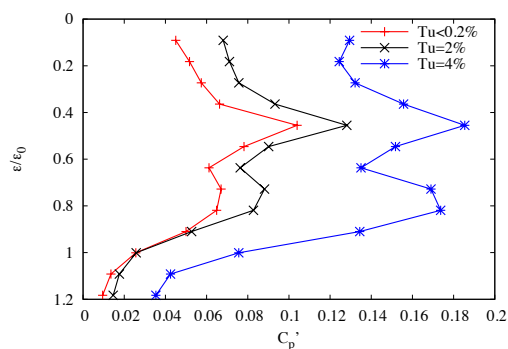


Figure 3. Evolution of C_p' along the $\frac{\epsilon}{\epsilon_0}$ axis on the L_2 line

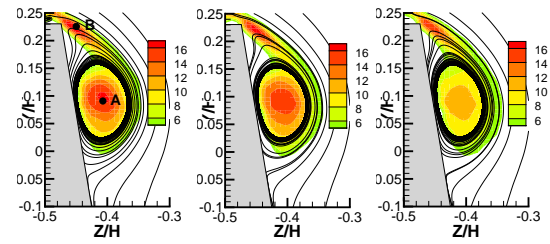


Figure 4. "2D Streamlines" and isocontours of vorticity. $Tu=0.2\%$ (left), $Tu=2\%$ (center), $Tu=4\%$ (right)

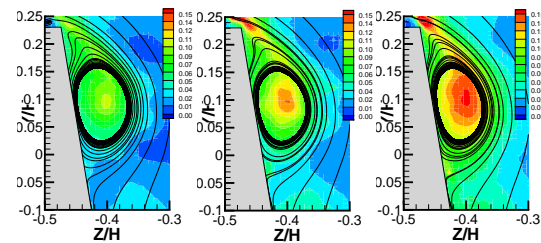


Figure 5. "2D Streamlines" and isocontours of turbulent kinetic energy. $Tu=0.2\%$ (left), $Tu=2\%$ (center), $Tu=4\%$ (right)

	u^2/U_∞^2		v^2/U_∞^2		w^2/U_∞^2		vw/U_∞^2	
Tu	A	B	A	B	A	B	A	B
0 %	.104	.147	.065	.032	.029	.025	.017	-.005
2 %	.134	.212	.095	.039	.034	.041	.017	-.011
4 %	.107	.243	.151	.047	.035	.043	.023	-.016

Table 1. Reynolds stresses values. (A): vortex center, (B) :Shear layer (see fig. 4)

Spatio-temporal properties of the primary vortex

It is now necessary to study the frequency content of the fluctuating pressure signal in order to understand which flow structure may be associated with the evolutions of C'_p . We will concentrate our discussion on special pressure taps locations which are characteristics of the dynamic of the flow: one located near the sharp edge ($\frac{\epsilon}{\epsilon_0}=0.18$) and one located at the mean second separation point ($\frac{\epsilon}{\epsilon_0}=0.44$) (Figures 6 and 7). The results are presented in function of the Strouhal number defined as: $St = \frac{f \cdot H}{U_\infty}$ where U_∞ is the free-stream velocity and H , the height of the model, about equal to the length of the conical structure. In the presence of FST, the frequency content is significantly changed. This means that the flow structure associated to the high level of C'_p is different. Just below the shear layer, in a region of

August 28 - 30, 2013 Poitiers, France

”dead water” ($\frac{\varepsilon}{\varepsilon_0} = 0.18$), FST imposes a large band contribution centered around $St \approx 1.5$ while no clear contribution appears without FST. We can then assume here that this area of the flow is submitted to large pressure fluctuations due to a modification of the unsteady outer-flow separating over the A-pillar in a flapping shear layer. A significant part of the fluctuating pressure is therefore believed to be due to a contribution of the unsteady aerodynamic field induced by the moving boundary of the lateral rolling shear layers. The DSP obtained at the maximum mean pressure gradients show a similar trend to that obtained just below the shear layer with a dominant broadband contribution centered around $St \approx 0.9$.

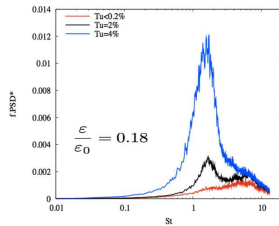


Figure 6. Wall pressure spectrum at $\frac{\varepsilon}{\varepsilon_0} = 0.18$

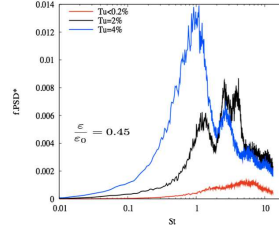


Figure 7. Wall pressure spectrum at $\frac{\varepsilon}{\varepsilon_0} = 0.45$

The frequency content of the velocity field has been studied. For brevity, only the results obtained on a line parallel to the wall passing through the vortex center are presented. The results obtained and analysed are the same whatever the chosen area in the velocity field. Spectra of the V component of the velocity are plotted in Figures 8, 9 and 10 as function of the frequency and of y coordinate. These velocity spectrum clearly show that as in the pressure spectrum, the presence of FST impose a large band contribution centered around $St \approx 2$ for $Tu = 2\%$ and $St \approx 1.5$ for $Tu = 4\%$. This decrease of the meandering frequency of the vortex with the increase of the integral length scale seems to validate the hypothesis that the meandering is triggered by the external turbulence. However, there is no direct link between the integral length scale of FST and the meandering frequency present in the spectrum. Indeed, the presence of the model leads to a modification of the turbulence scales contained in the FST (Bearman & Morel (1983)). One may remark that more one goes down the structure more the meandering frequency is low. This may be explained by the fact that the flows encountered in the shear layer and near the reattachment point have not the same history. In the shear layer, the frequency content is greatly dependant of the frequency content of the boundary layer in the facing ramp whereas in the vortex center the interaction with the external flow is greater which may leads to a modulation of the meandering frequency. Although not shown in the paper, spectra of the W component present similar trends, but in a lower frequency range.

To deepen this analysis, we studied the spatial pressure-pressure correlation defined as: $R_{pp}(\varepsilon_r/\varepsilon_0, \varepsilon/\varepsilon_0) = \frac{\langle p(\varepsilon_r/\varepsilon_0) \cdot p(\varepsilon/\varepsilon_0) \rangle}{\sqrt{\langle p(\varepsilon_r/\varepsilon_0)^2 \rangle} \cdot \sqrt{\langle p(\varepsilon/\varepsilon_0)^2 \rangle}}$ (figure 11). The reference point is $\frac{\varepsilon_r}{\varepsilon_0} = 0.79$. ε_r corresponds to the position of the maximum of C'_p in the presence of FST. The figure 11 shows that the pressure correlation is very similar with and without FST for $\frac{\varepsilon}{\varepsilon_0} \geq 0.53$ which corresponds to the location of the primary vortex core.

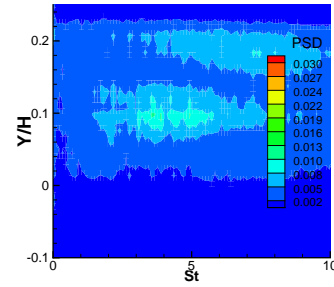


Figure 8. PSD of fluctuating velocity along a vertical line through the primary vortex center. $Tu = 0.2\%$

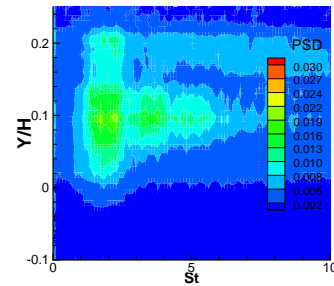


Figure 9. PSD of fluctuating velocity along a vertical line through the primary vortex center. $Tu = 2\%$

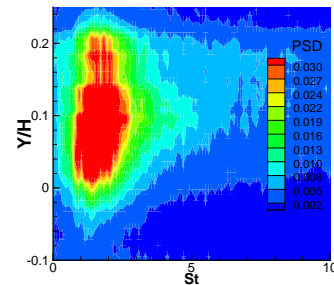


Figure 10. PSD of fluctuating velocity along a vertical line through the primary vortex center. $Tu = 4\%$

For $\frac{\varepsilon}{\varepsilon_0} \leq 0.53$, the evolution of the correlation coefficient is very different with and without FST. Indeed, whereas for the uniform free-stream case, no spatial correlation is extracted, in the presence of FST, a negative correlation is detected. The absence of spatial correlation without FST may be interpreted as the signature of the presence of two vortices. On the contrary, the spatial coherence detected with is the signature of the global response of the separated region perturbations.

Study of vortex dynamics POD Analysis

To educe part of the spatio-temporal properties of the conical vortices, a Proper Orthogonal Decomposition of the PIV velocity fields was carried out. The domain on which POD is performed is restricted to $z/H < -0.2$, $-0.15 <$

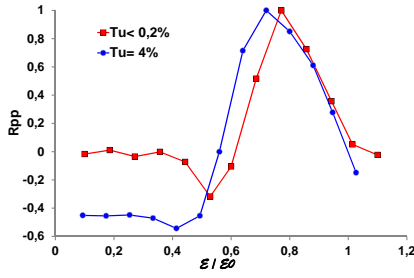


Figure 11. Spatial pressure-pressure correlation. The pressure reference point is $\frac{\varepsilon}{\varepsilon_0} = 0.79$.

$y/H < 0.3$ (the lower bound of z is fixed by the PIV measurements). The direct method is applied to the three components of the velocity, and a decomposition of the form:

$$U_i(X, t) = \bar{U}_i(X) + \sum_n a_n(t) \Phi_i^{(n)}(X)$$

is classically obtained for each dataset (each turbulence intensity), where a_n are the temporal coefficients, and Φ^n are the modes which depend on $X = (z/H, y/H)$. The eigenvalues $\lambda_n = \overline{a_n^2}$, normalised with the total energy, are plotted in Figure 12 for each turbulence intensity as a function of the mode number, in a log-log scale. It is clearly seen that the percentage of energy contained in the first modes, increases with the free-stream turbulence. Beyond mode number 10, the energy of the modes decreases roughly with the same slope for each dataset. Spectra of the coefficient a_1 for each free-stream turbulence are plotted in Figure 13. A clear broadband contribution is identified around the same St than the meandering frequency identified using pressure and velocity ($St \simeq 1.5$ for $Tu = 4\%$ and $St \simeq 2$ for $Tu = 2\%$). It is therefore expected that a reconstruction using the first modes will help to characterise this large scale motion of the vortex.

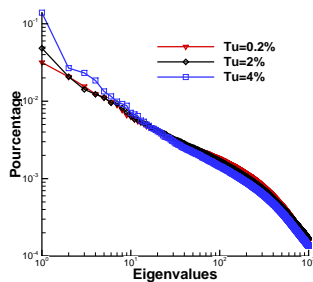


Figure 12. Eigenvalues $\lambda_n = \overline{a_n^2}$ normalised with the total energy

The goal of the following section is to analyse the meandering motion more quantitatively, using different characteristics of the vortex. It is therefore convenient for this task to filter out the smaller scales of the flow. Figure 14 shows an example of a reconstruction using 10 modes, compared with the instantaneous field. One can see that small scales

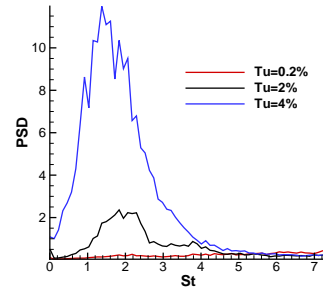


Figure 13. Frequency spectrum of the first coefficient (a_1) obtained by POD analysis

are well filtered out by POD and that the larger scales are well reproduced. Although a quantitative criterion should be used to select the number of modes necessary for the extraction of the meandering motion, visual inspection of the fields suggest that the following results are not significantly altered by the choice of the number of modes. Therefore, a reconstruction of the field using the 10 first modes is used in the following.

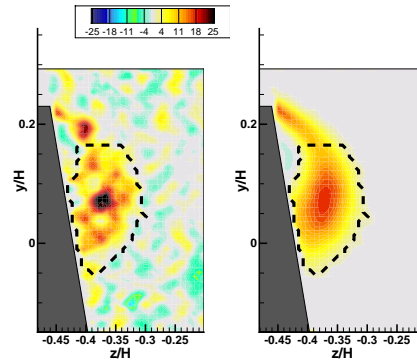


Figure 14. Instantaneous field of vorticity for $Tu=4\%$: (left) Raw field, (right) With a 10 POD mode filtering

Temporal analysis of vortex meandering

Figure 15 shows the iso-surface of the axial vorticity component normal to the measurement plan in the spatio-temporal domain (y, z, t) . The vorticity was here calculated using the POD-filtered velocity field. For each free-stream turbulence, a sequence of 200 instantaneous fields was chosen arbitrarily. This representation shows in a qualitative way that the coherence of the structure is becoming smaller when the free-stream turbulence increases. Indeed, one may observe that, with $Tu = 4\%$, the vortex presents strong variation in position and intensity.

In order to analyse more quantitatively the dynamic of the vortex, the region where $\omega_x \geq 2$ (computed from the reconstructed fields) was first identified. Then, in order to separate the rolling shear layer from the primary vortex, this region was cut at the y where a saddle point was detected in the vorticity fields, as show on Fig. 14. The center of the primary vortex was then defined as the barycenter based

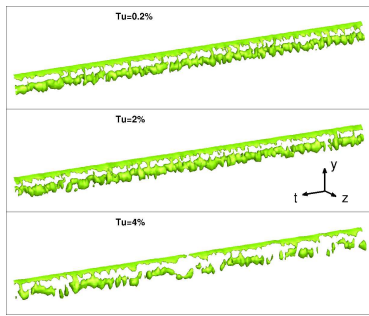


Figure 15. Spatio-temporal evolution of the primary vortex. Isosurface: $\omega_z = 12$

on the vorticity in this region. As this was done for every instantaneous field, this allowed to follow the position of the vortex in time. No preferential motion was observed and the vortex trajectory seems rather erratic. This observation is in good agreement with the study of Levy et al (2013), without FST.

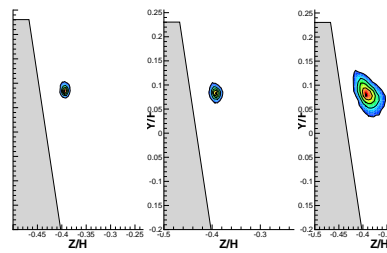


Figure 16. Location Probability Density function of the primary vortex center for the three turbulence levels

Figure 16 shows the pdf of the location of the primary vortex. Three observations can be made from this pdf: (i) The pdf spread increases with the turbulence intensity. It seems logical in light of the spatio-temporal evolution of the structure observed on figure 15 (ii) Whatever the turbulence intensity, the pdf has not a gaussian shape contrary to what might be observed without the presence of the wall (delta wings at incidence for example). The main direction of the vortex displacement seems to be parallel to the wall. (iii) The most probable location of the vortex is different from the location of the center of the vortex in the mean velocity fields, as already noticed by Levy et al(2013). An important difference with the study of Levy et al(2013), however, is that no precession movement can be identified using the pdf. It is not clear whether this difference is due to the inclination of the wall which is different in each study.

The spectrum of the primary vortex displacement (in the z-direction) is shown in figure 17.

A large band contribution is present whatever the turbulence level. As expected, the intensity of this contribution is enhanced by the presence of FST. As observed on the velocity spectra (figures 8, 9 and 10), the center of the broadband contribution is shifted toward the low Strouhal number when Tu is increasing. According to the vortex dynamics, one may remark that the frequencies detected on the vortex center displacement are similar to those observed

on the spectrum of the v-velocity component ($St \approx 2$ for

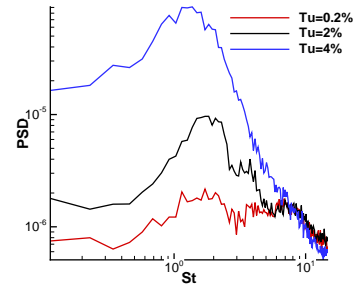


Figure 17. Frequency spectrum of the primary vortex center displacement in the z direction

$Tu = 2\%$ and $St \approx 1.5$ for $Tu = 4\%$). In the same manner, it has been observed a link between the spectrum of the w-velocity component and the spectrum of the vortex center displacement in the y-direction.

Conclusion and Perspectives

The effects of free-stream turbulence on the conical vortex structure generated by an A-Pillar were studied by combining Stereo-HS-PIV and multi-point pressure measurements. It has been shown that free-stream turbulence leads to a modification of the dynamic of the A-pillar vortex and of the resulting wall pressure field. Concerning the sidewall, the fluctuating pressure is strongly increased with the presence of upstream turbulence. In presence of FST, the coefficient C_p' seems to be associated with a global modification of the 3D separation and induced aerodynamic field. Indeed, the significant amplification of the meandering of the structure observed highlights the high receptivity of this structure to perturbations generated by external turbulence. We therefore believe that the comprehension of the influence of FST on this unsteady aerodynamic is a necessary step to develop control strategies adapted to the nature of the upstream flow. To complete the analysis, numerical simulations (DDES) will be performed for the same geometry, with different turbulence levels generated upstream the body. Provided that the phenomena observed in the experiment are well reproduced in the simulations, the access to the whole velocity and pressure fields should allow a better characterisation of the flow structures and their dynamic.

REFERENCES

- Alam F.,Watkins S., Zimmer G. (2003) Mean and time-varying flow measurements on the surface of a family of idealized road vehicles. *Exp. Therm. Fluid Sci.* (27), 639-654, Elsevier Science.
- Bearman P.W; and Morel T. (1983): Effect of free stream turbulence on the flow around bluff bodies, *Prog. Aerospace Sci.* 20: 97-123.
- Comte-Bellot G, Corrsin S. (1966) The use of contraction to improve the isotropy of a grid generated turbulence. *Journal of fluid mechanics* ; 25: Part 4.
- Hoarau C., Borée J., Laumonier J., Gervais Y (2008). Unsteady wall pressure field of a model A-pillar conical vortex. *Int. Journal of Heat and Fluid Flow*; 29 : 812-819
- Levy B., Brancher P. (2013) Topology and dynamics of the A-pillar vortex. *Phys. Fluids* 25; 037102